Available online at www.sciencedirect.com
ScienceDirect
Acta Materialia 54 (2006) 4111–4127
Acta MATERIALIA
www.actamat-journals.com

Ultrafine-grain-sized zirconium by dynamic deformation

B.K. Kad [a], J.-M. Gebert [b], M.T. Perez-Prado [c], M.E. Kassner [d], M.A. Meyers [a,*]

[a] *Department of Applied Mechanics and Engineering Science, University of California, 9500 Gilman drive, San Diego, La Jolla, CA 92093-0411, USA*
[b] *Institute of Materials Science I, University of Karlsruhe, Germany*
[c] *Centro Nacional de Investigaciones Metalúrgicas (CENIM), 28040 Madrid, Spain*
[d] *University of Southern California, Los Angeles, CA 90089, USA*

Received 19 May 2005; received in revised form 23 March 2006; accepted 27 March 2006
Available online 8 August 2006

Abstract

A polycrystalline zirconium alloy (Zircadine 702, containing 0.7% Hf) was subjected to high plastic strains (shear strains of 25–100) at a high strain rate ($\sim 10^4\ s^{-1}$) in an experimental setup comprising of a hat-shaped specimen deformed in a split Hopkinson bar. A narrow region of intense plastic deformation (10–25 μm thick) is produced which was analyzed by scanning (electron backscattered diffraction) and transmission electron microscopy. The microstructure within the shear band is characterized by equiaxed grains with an average size of 200 nm. The temperature excursion undergone by the deforming region is calculated on the basis of a Zerilli–Armstrong constitutive equal channel. The calculated temperature for a shear strain of 100 is equal to 930 K, corresponding to $0.43T_m$. Electron backscattered diffraction reveals that plastic deformation by shear leads to a strong $\langle 1\,1\,\bar{2}\,0\rangle$ fiber texture prior to the breakup of the existing grain structure. The ultrafine-grain structure observed is similar to that obtained in conventional severe plastic deformation processes such as equal channel angular extrusion, suggesting that the mechanism of grain refinement is the same in both processes, in spite of the differences in strain rate and thermal excursion. A mechanism is proposed for the breakup of the existing equiaxed microstructure (with grain size ~14 μm) into an ultrafine structure. It has three stages: (1) formation of elongated cells and subgrains; (2) increased misorientation between neighboring grains and breakup of elongated grains into smaller units; and (3) rotation of boundaries by grain boundary rotation and formation of equiaxed structure.

Keywords: Shear bands; Ultrafine grains; Severe plastic deformation; Zirconium; Dynamic deformation

1. Introduction

Polycrystalline metals with grain sizes in the submicrometer or nanometer range exhibit a range of interesting properties including a higher electrical resistance, higher diffusion coefficient, and higher strength (e.g., Refs. [1–6]). A promising method to produce bulk nano- or submicrometer polycrystalline metals is by severe plastic deformation (SPD), where the material undergoes large plastic strains. Although this phenomenon has been known for some time (e.g., Ref. [7]), different technologies are under development, e.g., torsion straining under hydrostatic pressure (HPT; e.g., Refs. [8–15]) and equal channel angular pressing or extrusion (ECAP or ECAE; e.g., Refs. [16–22]). The mechanisms that contribute to the strong grain refinement in SPD are the subject of much investigation worldwide. Interestingly, it is well known that adiabatic shear bands, an important deformation mode at high strain rates, undergo large plastic strains and that the resulting microstructure often consists of ultrafine equiaxed grains (e.g., Refs. [23–39]). The objectives of this research program were (1) to investigate whether the concentrated plastic deformation in a shear band in zirconium can yield microstructures similar to those being obtained in SPD and (2) to establish whether the mechanisms of microstructural evolution are similar in the two processes.

* Corresponding author. Tel.: +1 6195345698/07.
E-mail address: mameyers@mae.ucsd.edu (M.A. Meyers).

1359-6454/$30.00
doi:10.1016/j.actamat.2006.03.053

2. Experimental

2.1. Material

Commercially pure zirconium (Zircadine 702) was purchased from Teledyne Wah Chang, Albany (Oregon). It was received in a cold-worked condition as a rod 25.4 mm in diameter. Table 1 shows the chemical composition of the material provided by the manufacturer. The mechanical properties of the as-received material, also provided by the manufacturer, were the following: yield strength = 352 MPa; tensile strength = 492 MPa; and elongation = 26%.

2.2. Specimens for mechanical testing

Two specimen geometries were utilized in this study: hat-shaped and cylindrical specimens. Cylindrical specimens were used to obtain the quasi-static and dynamic mechanical response of the material. Compression tests were performed on cylindrical specimens to estimate the dependence of the yield strength on the strain rate. The cylinders had a length of 8 mm and a diameter of 5 mm.

Hat-shaped specimens were used to generate high shear strains in a localized region. Fig. 1(a) illustrates the dimensions of the hat-shaped specimens. This design was created by Meyer and Manwaring [40] and has been used for the formation of adiabatic shear bands in steel [26], titanium [23–25,28], copper [27,29], tantalum [30–33], aluminum alloy [34], and stainless steel [35]. This specimen shape provides ideal conditions to concentrate a high shear stress that results in the formation of shear bands. Three different specimen hat heights were used: $x = 0.75$, 1, and 2 mm. Thus, the deformation time in the shear region, calculated by dividing the hat displacement by the velocity, is of the order of 0.05–0.1 ms. The velocity of the striker bar was not measured when the experiments were performed, but was calculated to be approximately 26 m/s [41]. The dimensions of the specimen shown in Fig. 1(a) are: $d_0 = 10.15$ mm; $d_1 = 9.98$ mm; $h = 4.80$ mm; $L = 10$ mm; and $D = 19.10$ mm. The total length of the specimen was kept constant at 10 mm. Table 2 shows the heights used, the corresponding cross-sectional areas where the deformation is concentrated, and the expected strains assuming that the total strain is concentrated in the shear band with a thickness of 20 μm.

Table 1
Chemical composition of the as-received material

Element	Composition			PPM
	Top (wt.%)	Middle (wt%.)	Bottom (wt.%)	
Zr	>99.146	>99.055	>99.046	
Hf	0.6	0.7	0.7	
Fe + Cr	0.1	0.09	0.09	
H	<0.0003	<0.0003	<0.0003	5
N	0.004	0.005	0.004	36
C	0.02	0.01	0.02	
O	0.13	0.14	0.14	1300

Dynamic compression tests (on both cylindrical and hat-shaped specimens) were performed in a Hopkinson bar (e.g., Ref. [42]). A bar diameter of 20 mm and striker with lengths of 75, 125, and 250 mm were used. The tests were performed at room temperature and the strain rate was varied from $\dot{\varepsilon} = 10^{-3}$ up to 3×10^3 s^{-1}. A typical test profile is shown in Fig. 2. The quasi-static experiments were performed using a Satec testing machine (model T20000). A load cell recorded the force, and the displacement was measured using an extensometer.

2.3. Microstructure characterization

The microstructures of the as-received material, as well as those of the deformed specimens, both outside and within the shear band region, were characterized using optical microscopy (OM), electron backscatter diffraction (EBSD), and transmission electron microscopy (TEM).

Fig. 1(b) shows how the specimens were cut for microstructural examination. They were cut in two directions, both parallel and perpendicular to the shear direction. A diamond saw at a speed of 600 rpm and a feed speed of approximately 0.01 mm/s was used.

Sample preparation for OM included, first, grinding in an automated polishing machine, using SiC papers of grit sizes ranging from 600 to 4000, and an applied force between 10 and 50 N. The samples were then etched using a solution containing 45 vol.% H_2O, 45 vol.% HNO_3, and 10 vol.% HF. A cotton pad was soaked in this solution and swabbed with light pressure for approximately 5–15 s on the polished surface. A final anodization step followed in order to improve the contrast between grains and protect the surface from oxidization. The anodization solution contained 60 ml absolute ethanol, 35 ml H_2O, 20 ml glycerine, 10 ml 85% lactic acid, 5 ml 85% H_3PO_4, and 2 g citric acid. The voltage was kept constant at 20 V and the specimen was contacted with the anode for less than a second. The anodization resulted in a light golden layer. The optical microstructure of the shear band and its overall profile are shown in Fig. 3.

EBSD (e.g., Refs. [43–45]) examination was performed in undeformed regions and in areas close to the shear band in specimens deformed using the three displacements (0.75, 1, and 2 mm). Measurements were carried out in a JEOL scanning electron microscopy (SEM) instrument operating at 20 kV using Oxford Instruments INCA software. The samples were placed in the SEM sample holder as shown in Fig. 1(c), i.e., the normal, transverse, and shear (longitudinal) directions in the EBSD maps and pole figures correspond to the axes marked ND, TD, and SD. Sample preparation for EBSD included the grinding step described above and subsequent mechanical polishing with a solution of 0.3 μm alumina (10 g) in 150 ml H_2O and finally 0.05 μm alumina (5 g) in 150 ml H_2O. Finally, the etching procedure detailed above was performed for optimum surface finishing.

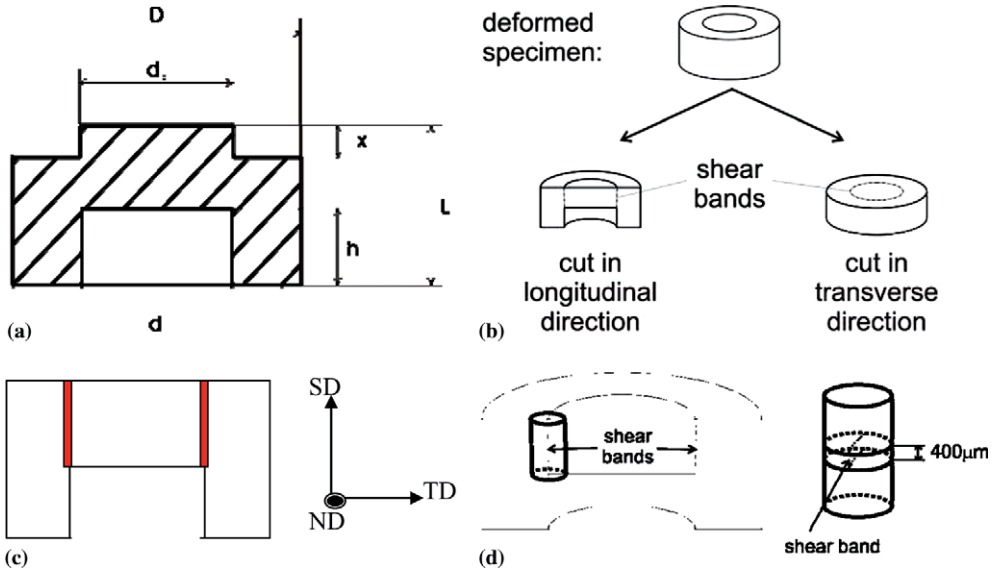

Fig. 1. Hat-shaped specimen geometry used in the dynamic deformation tests.

Table 2
Specimen hat heights employed and predicted strains

Height of the specimen hat (x)	Cross-sectional area (mm^2)	Expected strain $\gamma = \frac{\text{height of hat}}{\text{shear band thickness}}$
0.5	148.6	25
0.75	140.7	37.5
1	132.8	50
2	101.2	100

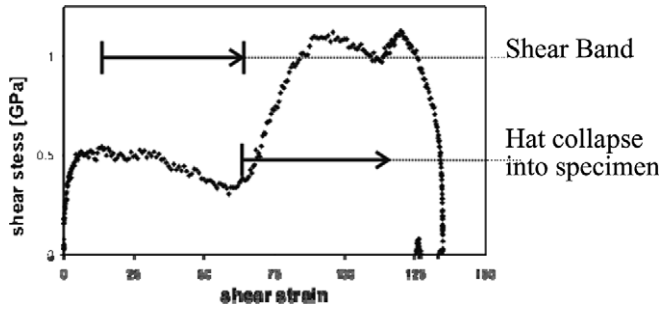

Fig. 2. Shear stress–displacement curve for the specimen with a hat height displacement of 0.75 mm.

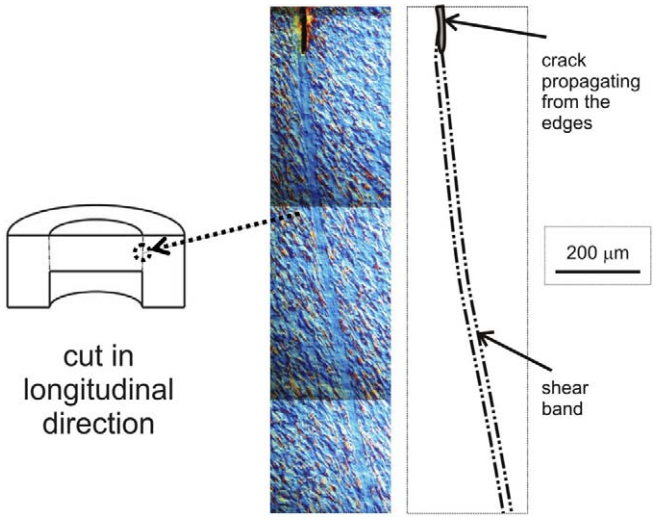

Fig. 3. Optical micrograph of shear bands in deformed hat specimen (hat height = 1 mm).

Specimens for TEM examination were obtained from cylinders of 3 mm in diameter that were cut out of the specimen as shown in Fig. 1(d). Disks of around 400 μm thickness were then cut out of each cylinder using electrical discharge machining (EDM) techniques. The disks were then thinned down using a 1200 grid SiC paper to a thickness of approximately 150 μm. Final thinning to electron transparency was achieved by electropolishing in a solution containing 90 vol.% acetic acid and 10 vol.% perchloric acid. The voltage was kept constant at 20 V and the polishing was performed at room temperature. The large strain accumulation in the shear band almost ensures that its polishing characteristics are strikingly different from those of the matrix. In the event that the shear band was ideally situated in the center of the TEM disk, perforation occurred at the shear band but is rapidly polished such that no thin area is observed. A more manageable alternative was to electropolish disks where the shear band is off-center. Looking at Fig. 3, we note that the shear band is slightly curved and thus its precise location varies along the length of the spark-machined rod. This geometrical factor facilitates the availability of numerous disks with off-center shear band. Such perforated foils were progressively ion milled in a Gatan PIPS unit at ambient conditions until the perforation grows to the edges of the shear bands. Fig. 4 shows OM and TEM images of the thin foil specimens. Fig. 4(a) and (b) show the low-magnification OM image of the TEM disk – clearly delineating the shear band as located at the edge of the perforated region. Such optical

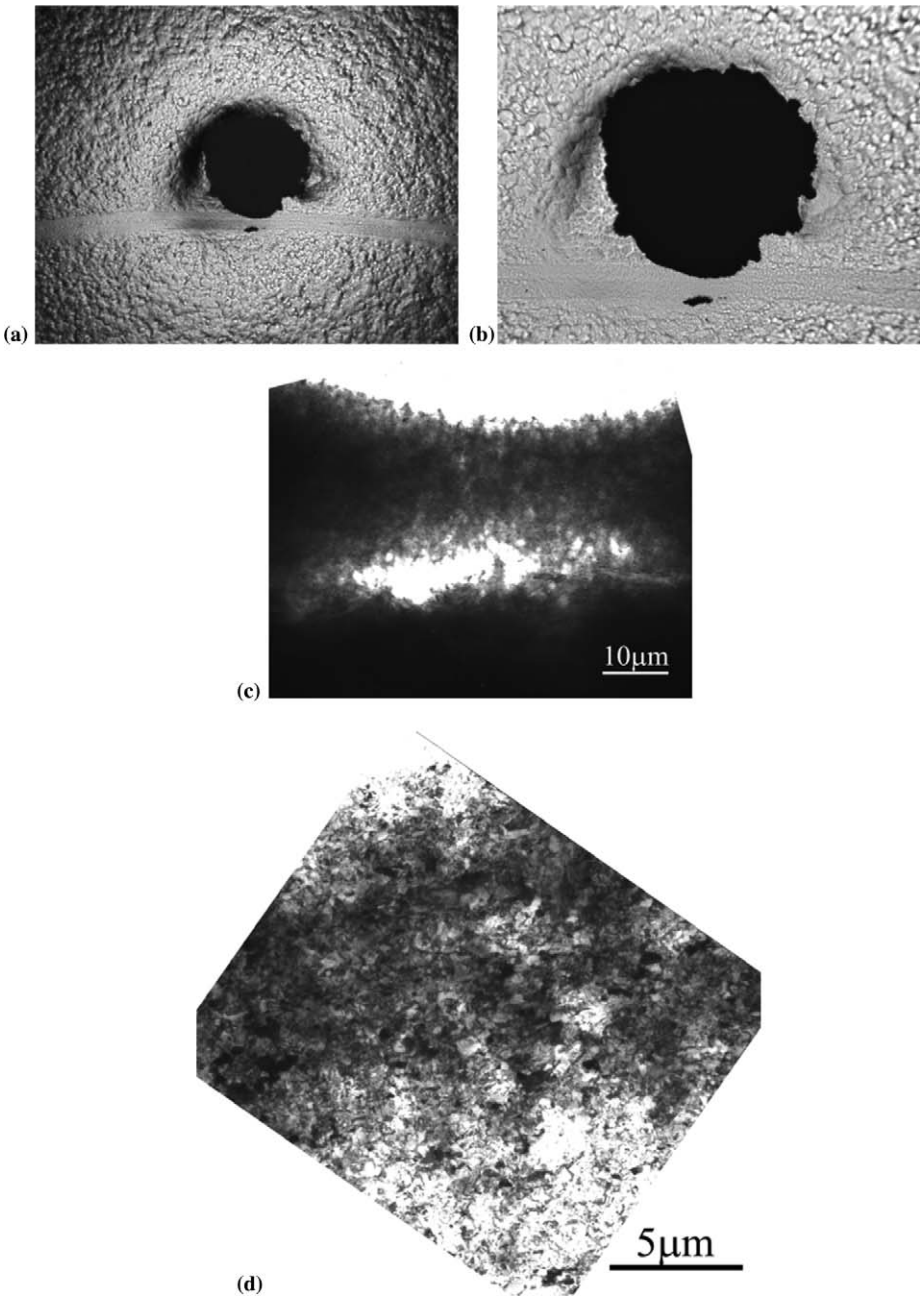

Fig. 4. Precision ion milling to extract the microstructural evolution in the shear bands. (a and b) Optical imaging of the shear band and (c) TEM imaging of the same perforation at the 15 μm wide shear band. (d) Preview of the fine-grain microstructure in the shear band.

examination was deemed essential to remove any ambiguity of the precise location being examined. Subsequent TEM examinations (Fig. 4(c) and (d)) reveal the additional information of fine grain size and texture as discussed later in Section 3.3. TEM observations were performed using a Philips CM30 microscope operating at 300 kV.

3. Results and discussion

3.1. Dynamic compression tests of hat-shaped specimens

A characteristic shear stress–shear strain curves, corresponding to a hat height of 1 mm, is illustrated in Fig. 2. The shear strength of the material is approximately 500 MPa. Softening due to shear localization can also be clearly appreciated starting at a shear strain $\gamma \approx 30$. The stress increase at a shear strain of 60 is due to the complete collapse of the head. Beyond that point, there is no significant amount of plastic deformation. Similar shear stress–shear strain curves were obtained for the remaining specimens, with different hat heights.

Fig. 3 shows a montage of OM images showing the full length of the shear band at one side of the hat-shaped specimen. Fig. 3 reveals that the shear band propagates along the direction of maximum shear stress. The microstructure within the shear band is not visible by OM. Grains adjacent

to the shear band are elongated toward the band. Therefore, plastic deformation also takes place outside of the shear band.

With increasing strain, the shear band width was found to increase as shown in Figs. 5 and 6. The shear band width varies between 6 and 14 μm for a hat displacement of 0.75 mm (Fig. 5) and between 8 and 24 μm for a hat displacement of 1 mm (Fig. 6). The shear band widths were measured both in the longitudinal (Fig. 6(a)) and transverse direction (Fig. 6(b)) and the results are, as expected, consistent. The maximum width of a single shear band observed was approximately 25 μm and occurred for a specimen with a 2 mm hat height. Occasionally, two parallel bands were distinguished.

Microindentation hardness measurements were made outside (far from the deformation area) and inside the shear band. The average of 10 measurements was taken at each location. The Vickers hardness value obtained within the band was 2.3 GPa; the hardness outside the band was 1.7 GPa. Assuming a Hall–Petch relationship it is possible to estimate the average grain size within the shear band:

$$\sigma_y = \sigma_0 + \frac{k}{\sqrt{d}} \tag{1}$$

The following relationship between hardness and yield stress was applied (e.g., Ref. [46]):

$$\mathrm{HV} = 3\sigma_y \tag{2}$$

By applying Eq. (1) both to the shear band region and to a non-deformed reference area, where the grain size is measurable, the term σ_0 can be eliminated and the value of the grain size within the shear band can be calculated:

$$\bar{d}_{\mathrm{SB}} = \left[\frac{k}{\frac{\mathrm{HV_{SB}}}{3} - \frac{\mathrm{HV_{ref.}}}{3} + \frac{k}{\sqrt{\bar{d}_{\mathrm{ref}}}}}\right]^2 \tag{3}$$

Elimination of σ_0 requires the assumption that the dislocation density is equal in both areas.

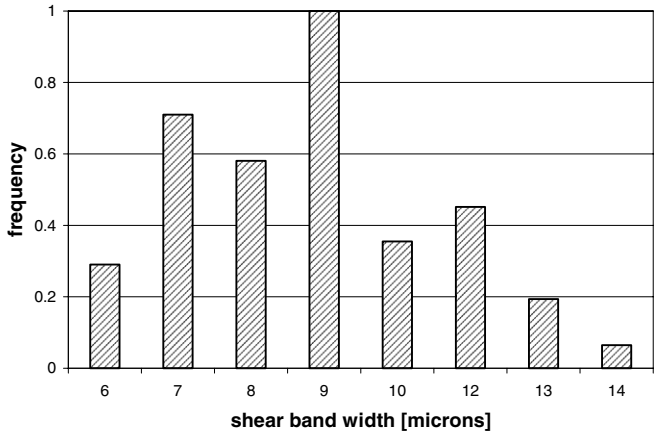

Fig. 5. Distribution of shear band thicknesses for hat height of 0.75 mm.

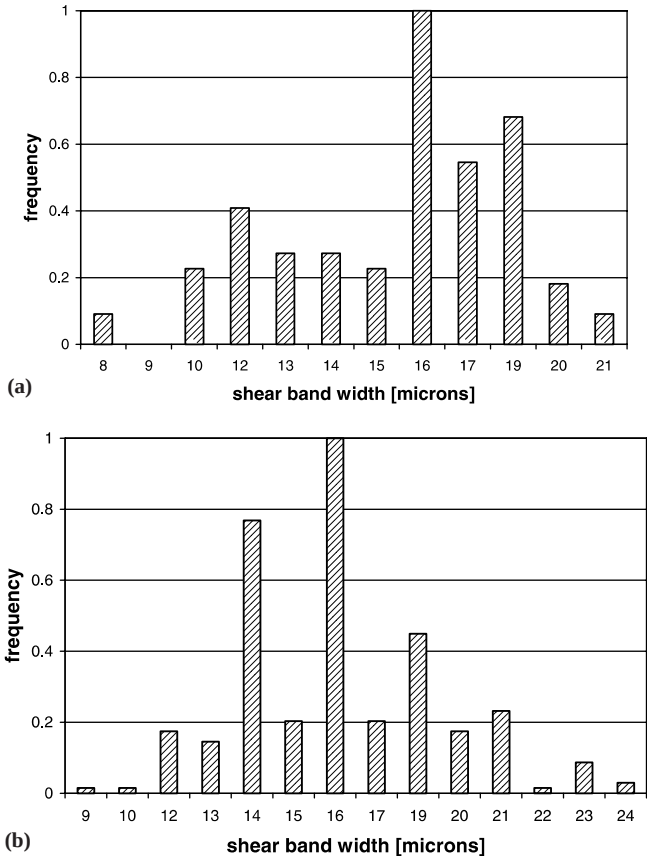

Fig. 6. Distribution of shear band thicknesses for hat height of 1 mm: (a) cut in longitudinal direction and (b) cut in transverse direction.

The Hall–Petch slope, k, obtained from Armstrong [47], is equal to 25 MN/m$^{3/2}$. The calculated value of d_{SB}, the grain size inside the shear band, is 0.7 μm. Due to the large temperature rise within the shear band, it is likely that the dislocation density is lower than in the reference area (where the material exhibits the initial, cold-worked condition). Therefore, this procedure provides an upper limit of the grain size.

Experiments performed at increasing gun pressures, ranging from 200 to 480 kPa, resulted in increasing shear band hardness. Table 3 summarizes the hardness values, number of measurements, and standard deviation values for each applied pressure. The pressure increase is directly related to the striker velocity, which, in turn, determines the strain rate. Thus, higher strain rate values apparently result in the formation of smaller grains within the band.

Table 3
Microhardness measurements to determine the strain rate dependence of the hardness inside the shear band

Gun pressure (kPa)	HVN (10 g)	No. of measurements	Standard deviation
200	207	33	18
350	239	36	24
410	251	54	20
480	265	69	19

3.2. Microtexture measurements using EBSD

Fig. 7 illustrates the EBSD maps corresponding to the normal direction (ND), transverse direction (TD), and extrusion direction or, later, shear direction (hereafter called SD) in an area outside the shear band (see Fig. 1(c) for the definition of ND, TD, and SD). It can be seen that the microstructure is formed by equiaxed grains of about 7.5 μm in diameter. The predominance of blue and green colors in Fig. 7(c) suggests the preferential alignment of prismatic directions along SD. Fig. 8 shows the inverse pole figures corresponding to ND, TD, and SD in the same area. Again, these figures reflect that, during extrusion, grains rotate until a prismatic direction becomes aligned with the extrusion direction (parallel to the shear direction, or SD). In fact, as can be seen in Fig. 8(c), SD spans the entire range of prismatic directions, between $\langle 10\bar{1}0\rangle$ and $\langle 11\bar{2}0\rangle$. A tendency of the *c*-axis to become parallel with the ND can also be inferred from Fig. 8(a). The preferential alignment of prismatic directions with the extrusion axis is characteristic of extruded hexagonal close-packed (hcp) alloys [48].

The texture evolution in the vicinity of the shear bands of specimens tested with hat displacements of 0.75, 1, and 2 mm was found to be similar. Thus, only the microtexture data corresponding to the specimen tested with a hat displacement of 0.75 mm will be shown. Fig. 9 illustrates the EBSD maps corresponding to the ND, TD, and SD directions. The black areas in the maps indicate regions where Kikuchi patterns could not be successfully indexed. This may be due either to the presence of a very high dislocation density or clusters of very fine grains (smaller than the resolution limit of the EBSD technique, about 0.2 μm). Grain elongation toward the shear direction in the vicinity of the band can be clearly appreciated. Additionally, grain fragmentation takes place as different slip systems operate in adjacent parts of each initial grain, thus leading to local lattice rotations in opposite directions [49]. The subdivision of grains is attributed to the formation of deformation-induced boundaries [53], which appear to be perpendicular

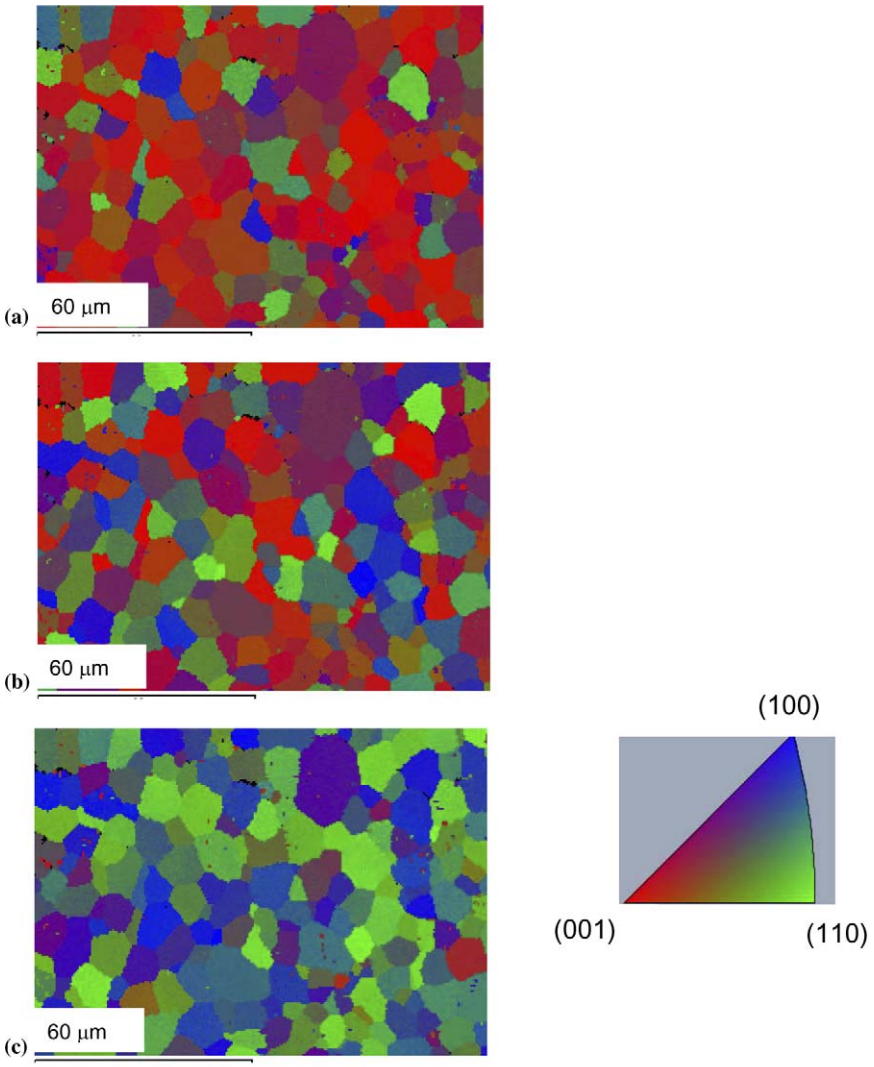

Fig. 7. EBSD maps corresponding to the (a) ND, (b) TD, and (c) SD directions (see Fig. 1(c)). The color coding used in the maps is illustrated in the inset.

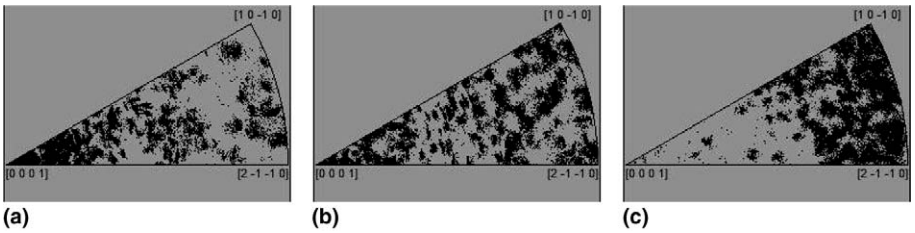

Fig. 8. Inverse pole figures corresponding to a non-deformed area: (a) ND, (b) TD, and (c) SD (=extrusion direction).

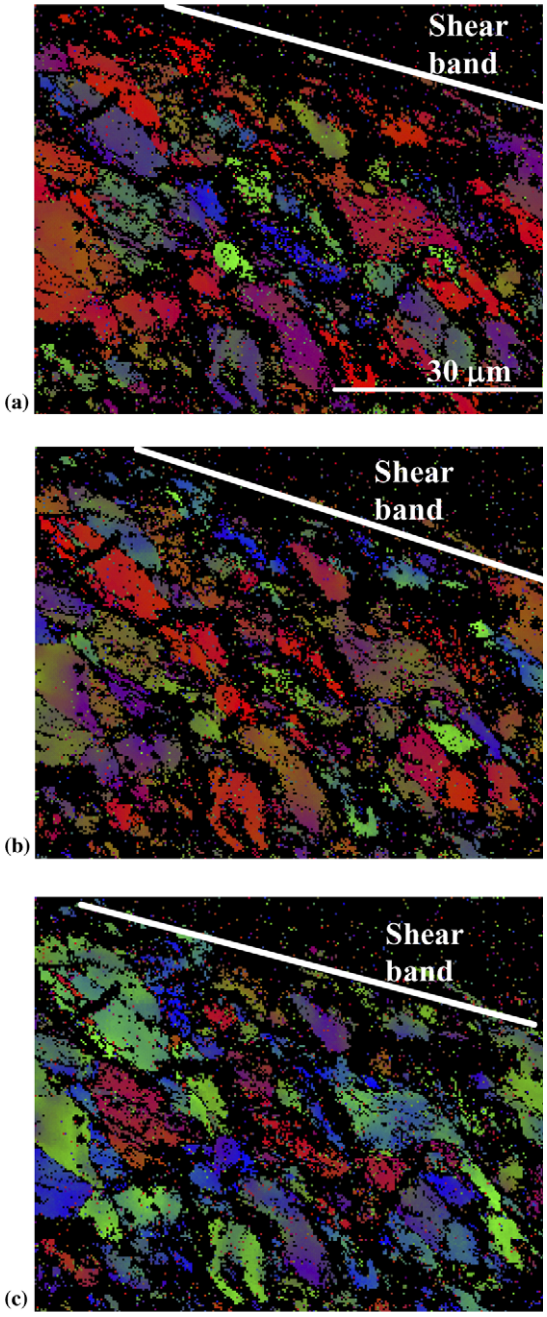

Fig. 9. EBSD maps corresponding to (a) ND, (b) TD, and (c) SD in the area close to the shear band. Same color coding as in Fig. 7. Hat displacement = 0.75 mm.

to the long direction of the elongated grains. Lattice distortion around these boundaries results in poor Kikuchi patterns and, thus, the appearance of black regions in the EBSD maps. The changes in colors within individual fragments indicate smoother lattice rotations.

The microtexture in the vicinity of the shear band is represented in Figs. 10 and 11 by means of the inverse pole figures corresponding to the ND (Fig. 10(a)), TD (Fig. 10(b)), and SD (Fig. 10(c)) as well as by the direct pole figures $(0\,0\,0\,1)$ (Fig. 11(a)), $(10\bar{1}0)$ (Fig. 11(b)), and $(11\bar{2}0)$ (Fig. 11(c)) directions. Significant texture changes can be noticed as a consequence of deformation. The lattice rotations taking place are apparent in the direct pole figures depicted in Fig. 11. These rotations seem to be predominantly around the ND axis (since the dot clusters elongate along concentric circumferences centered in the ND). Rotation angles as high as 30° can be noticed. Lattice rotations are also apparent in the inverse pole figures of Fig. 10. Furthermore, the main component of the texture is now a $\langle 11\bar{2}0\rangle$ fiber, where $\langle 11\bar{2}0\rangle$ directions tend to align with the SD and then there is cylindrical symmetry around this axis. This can be clearly appreciated in the clustering of SD poles around the $\langle 11\bar{2}0\rangle$ direction in Fig. 10(c). The intensity contours corresponding to the ideal $\langle 11\bar{2}0\rangle$ fiber have been superimposed in Fig. 12 to the measured direct pole figures. A good correspondence between the ideal fiber texture and the measured one can be observed. The formation of this fiber is attributed to the fact that the $\langle 11\bar{2}0\rangle$ direction is an "easy" slip direction in Zr crystals. Thus, as a consequence of the shear imposed, the grains in regions close to the shear band reorient until this slip direction becomes parallel to the shear direction, i.e., they rotate toward more stable orientations under the stress state imposed. However, the $\langle 11\bar{2}0\rangle$ fiber is not perfect, i.e., the volume fraction of grains rotated around the $\langle 11\bar{2}0\rangle$ (fiber axis) is not the same for all rotation angles. Instead, one specific orientation predominates: that with $(10\bar{1}0)$ planes parallel to the shear plane (SD–ND plane) (or, equivalently, with $\langle 10\bar{1}0\rangle$ directions parallel to TD) and thus *c*-axis parallel to ND. The prevalence of this specific texture component can be inferred from the clustering of ND poles around $\langle 0001\rangle$ in Fig. 10(a). Fig. 13 illustrates schematically several lattice orientations within the fiber, highlighting, among them, the predominant

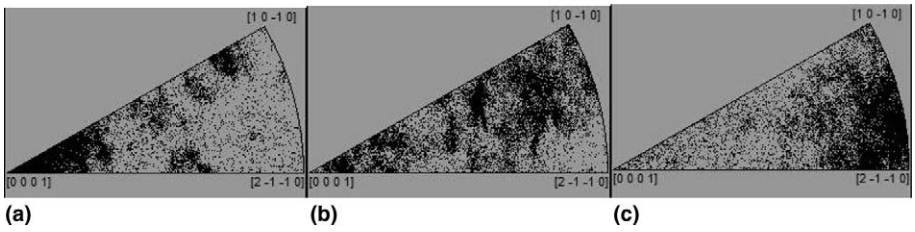

Fig. 10. Inverse pole figure corresponding to the area close to the shear band. Hat displacement = 0.75 mm: (a) ND, (b) TD, and (c) SD.

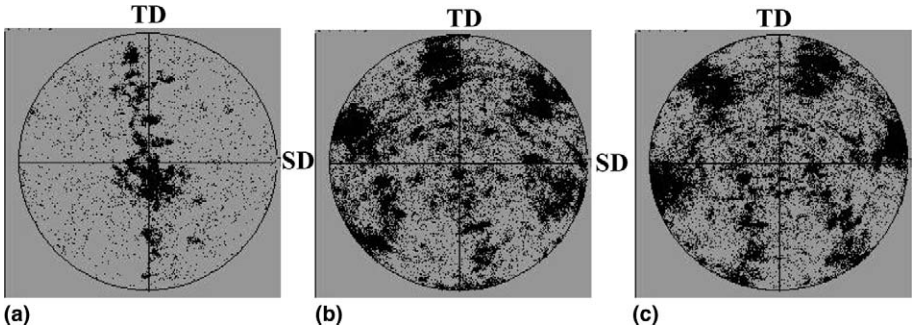

Fig. 11. Direct pole figures corresponding to the area close to the shear band. Hat displacement = 0.75 mm: (a) (0001), (b) $(10\bar{1}0)$, and (c) $(11\bar{2}0)$.

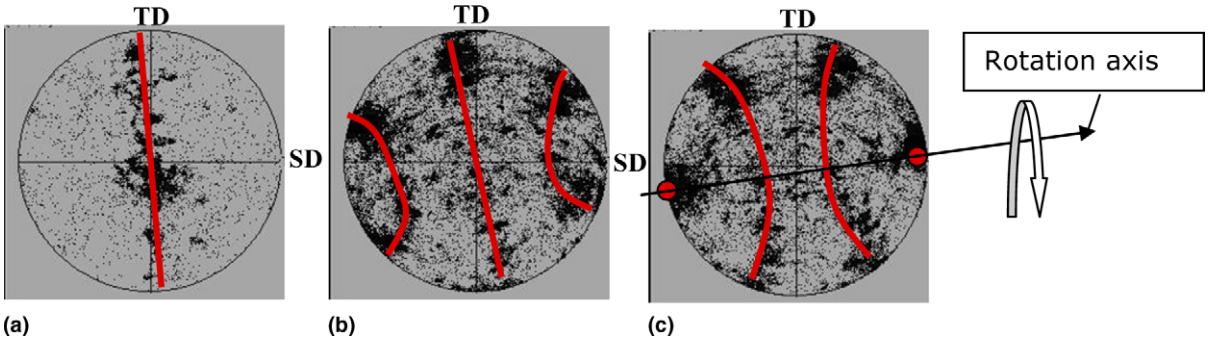

Fig. 12. Contours showing the ideal $\langle 11\bar{2}0\rangle$ fiber texture superimposed to the direct (a) (0001), (b) $(10\bar{1}0)$, and (c) $(11\bar{2}0)$ pole figures corresponding to the area close to the shear band (Fig. 9). Hat displacement = 0.75 mm.

orientation. The tendency of grains to rotate until a prismatic $(10\bar{1}0)$ plane is parallel to the shear plane is consistent with the fact that these crystallographic planes are favorable slip planes in Zr crystals.

In summary, examination of the texture evolution in the vicinity of the shear band is consistent with the activation of $\{10\bar{1}0\}\langle 11\bar{2}0\rangle$ slip systems. The formation of a fiber texture in the vicinity of shear bands has previously been observed in stainless steels [35] and tantalum [50] and it reflects the fact that, in addition to accommodating the imposed strain, neighboring grains must also achieve compatible deformation.

3.3. TEM examination

TEM was carried out on a number of specimens to study microstructural features of the shear bands. For consistency, we present only data for specimens tested at a gas gun pressure of 200 kPa using a 5-inch striker length, and in the interest of brevity, only selected results from the two extreme (i.e., the lowest and highest) strain conditions of 0.75 and 2 mm hat displacement ($\gamma = 30$ and 100, respectively) are reported here. The viewing direction is along SD (see nomenclature of Fig. 1(c)) for all results presented here. Fig. 4 gives a general overview of the process of tracking shear bands. The thin foils are perforated using electropolishing methods and then the perforation enlarged using incremental ion milling. Figs. 4(a) and (b) are optical micrographs of the TEM disk. We note the shear band lies at the edge of the perforation. This provides a reasonable assurance that we are indeed probing the microstructure at the shear band and its immediate vicinity in our TEM investigations as shown in Figs. 4(c) and (d). Fig. 4(d) provides the first glimpse of the fine-grain microstructure formed in shear bands.

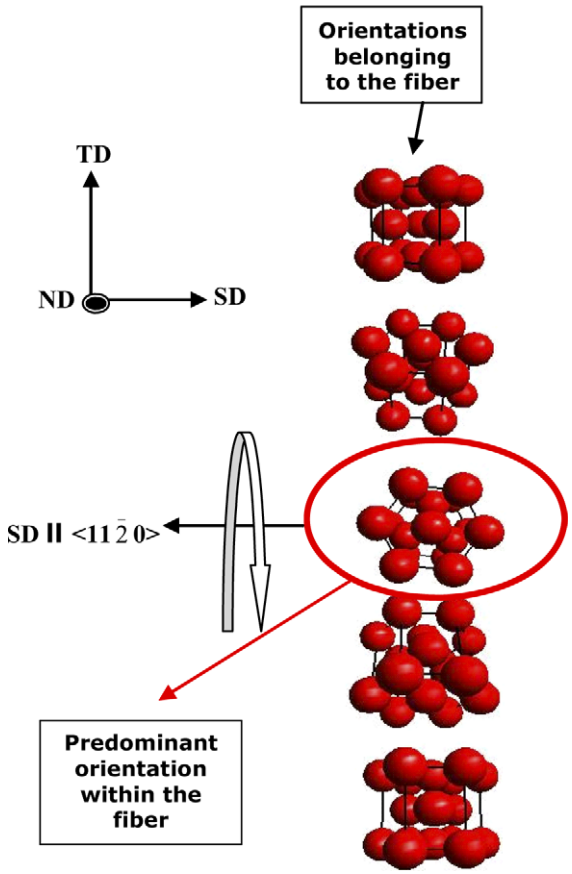

Fig. 13. Schematic of the main orientations present in the area close to the shear band. A non-perfect $\langle 11\bar{2}0\rangle$ fiber texture develops, where the predominant orientation is that with the *c*-axis parallel to ND.

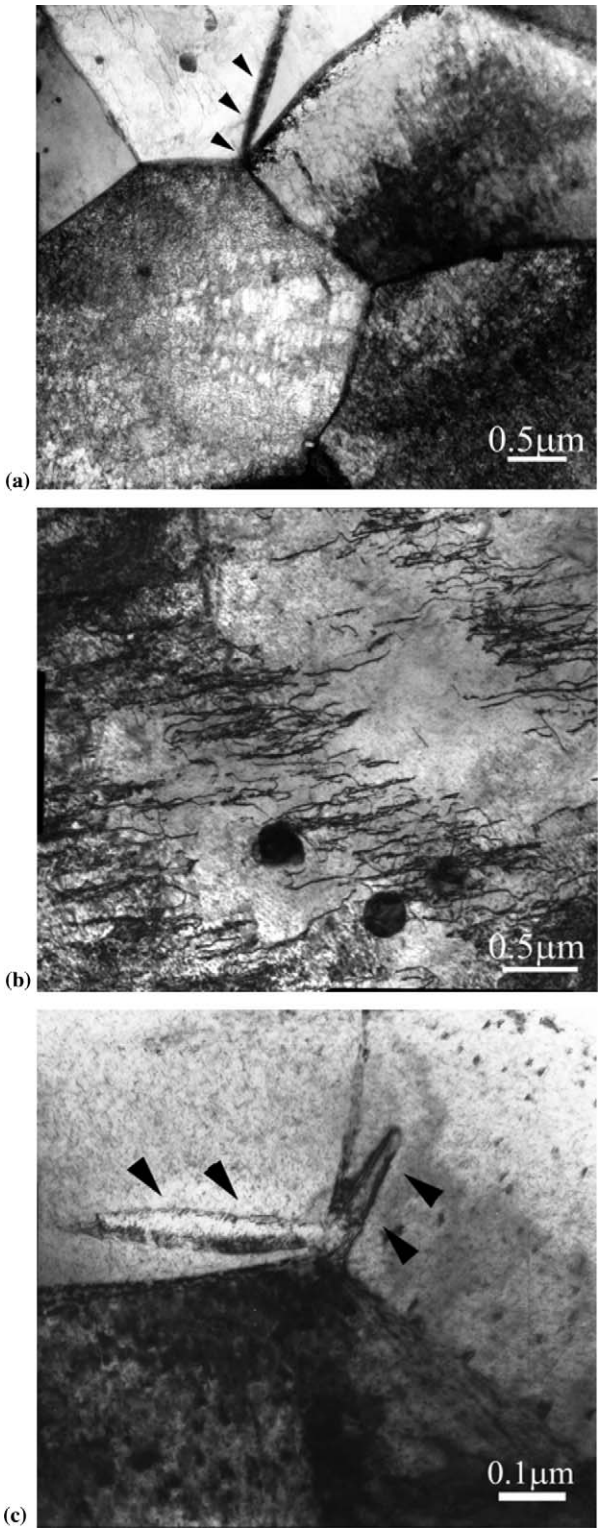

Fig. 14. Deformation substructure in (a) the vicinity of the shear band is comprised of (b) $\langle 11\bar{2}0\rangle$ lattice dislocation propagation and (c) twinning associated with grain boundaries.

3.3.1. Deformation characteristics in the vicinity of the shear band

We begin by examining the deformation microstructures in the vicinity (~100 μm from the shear band location) of the shear band. Fig. 14(a) shows the nominally equiaxed matrix microstructure undergoing deformation via both slip activity and twinning. The $\langle 11\bar{2}0\rangle$ dislocations gliding in the grain interior (Fig. 14(b)) contribute to slip. Twinning deformation, originating primarily at grain boundaries and vertices (see arrow in Fig. 14(a)), is also observed. Fig. 14(c) shows a particular grain vertex where multiple twinning variants are activated, in recognition of the less than 5 independent slip systems in hcp Zr. It is expected that such deformation modes contribute to the large-scale deformation of the shear band itself. We note that, despite the extent of deformation observed here, no finite grain shape changes are observed. As shown later such grain shape changes and rotations are confined to a narrow band at either side of the shear band and in most cases are about the size of the shear band width.

3.3.2. Deformation transitions from matrix to shear band

As we approach the shear band region, grain flow is observed where the initially equiaxed grains are compressed normal to the shear direction. Fig. 15(a) shows a composite micrograph of the shear band region (left) and the matrix on the right, separated by a narrow 2–5 μm transition region. As we approach the shear band region,

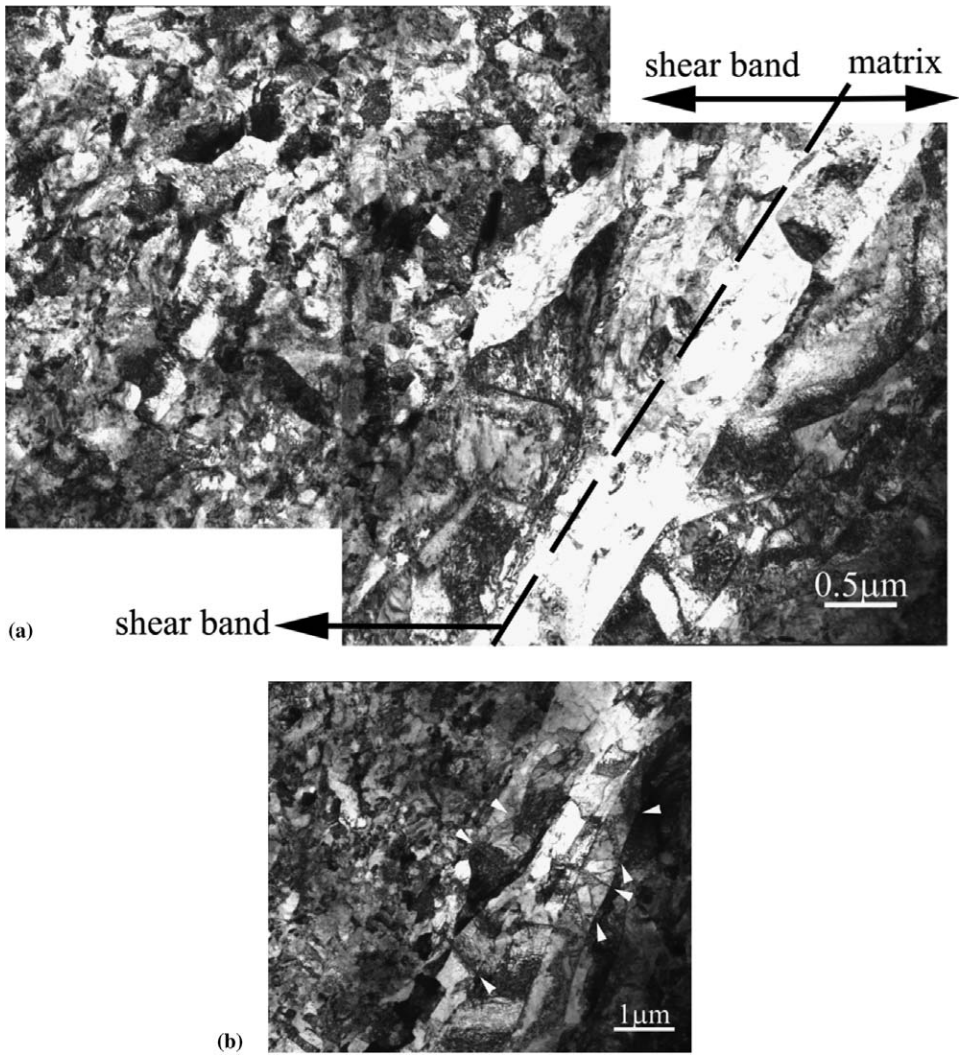

Fig. 15. (a) Composite of the shear band (left), matrix (right), and the matrix/shear band (dashed region) interface. The interface marks a sharp demarcation between the adjacent regions. (b) Fine details of deformation bands (arrows) along the pancake-like grain. Coarse grains evolve into a well-established fine-grained structure across a ~1 μm transition width.

grain flow is observed where the initially equiaxed grains are beginning to flow in the direction of imposed macroscopic shear (i.e., normal into the paper plane). Immediately outside the shear band, the grains retain their initial grain diameter (i.e., parallel to the shear band, see ND nomenclature in Fig. 1(c)), but are compressed across (TD) the shear band leading to the significant aspect ratio asperity observed in Fig. 15(a). Fig. 15(b) highlights some features of these elongated grains where deformation bands and twins (highlighted arrows, right) are operative in the elongated grain. Further to the left similar features (arrows) are shown to create distinct misorientations within the grain stretched along TD. Once inside the shear band region, the grains are commuted both along the ND and TD and we observed the appearance of an equiaxed microstructure of about 200 nm. Recall that the TEM viewing direction is along SD and both ND and TD are in the plane of the foil, such that commutation is observed nearly identical in directions orthogonal to SD.

3.3.3. Deformation features at low strain (x = 0.75 mm)

Fig. 16 shows a TEM micrograph of the shear band corresponding to a hat displacement of 0.75 mm. A sharp interface (dashed line, top left corner) delineates the matrix and the shear band. A nominal refined grain size of about 200 nm is observed within the shear band. However, the diffraction pattern (produced by placing the diffraction aperture over most of the shear band width) does not yield a ring pattern. The dominant diffraction spots (Fig. 16(b)) exhibit splitting or clustering (as indicated by white arrows) indicating that the orientations are nearly collinear. Such clustering also suggests the initial stages of grain breakup and minute orientation changes from bulk grain orientations. Satellite spots are construed as originating from minor tilts or rotations of small segments of the bulk grain.

3.3.4. Deformation features at high strain (x = 2.0 mm)

The composite micrograph of the matrix and shear band regions was shown earlier in Fig. 15. Fig. 17(a) shows the

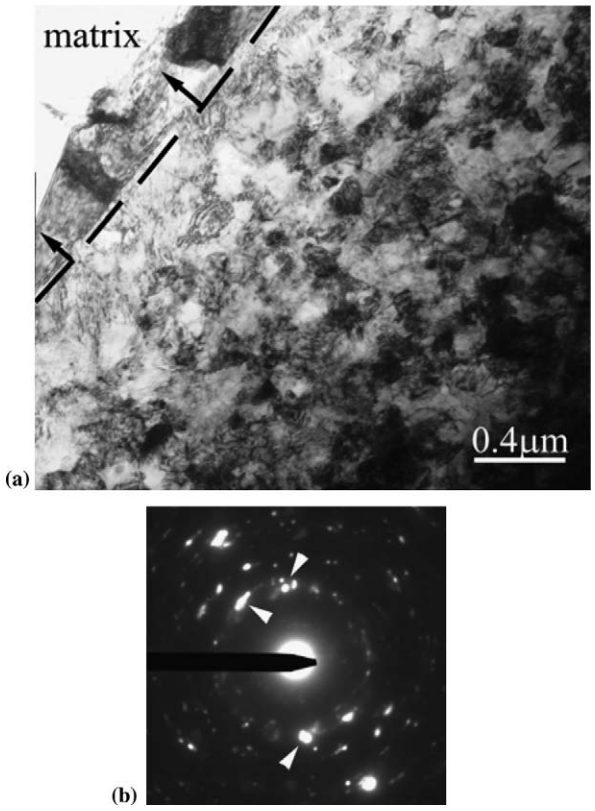

Fig. 16. Deformation shear band grain structure for hat displacement $x = 0.75$ mm: (a) overall view and (b) diffraction pattern. The microstructure reveals fine grains of ~200 nm. However, the diffraction pattern (produced by placing the diffraction aperture over most of the shear band width) does not yield a ring pattern but rather indicates the initial stages of minute orientation changes as observed by diffraction spot splitting (white arrows).

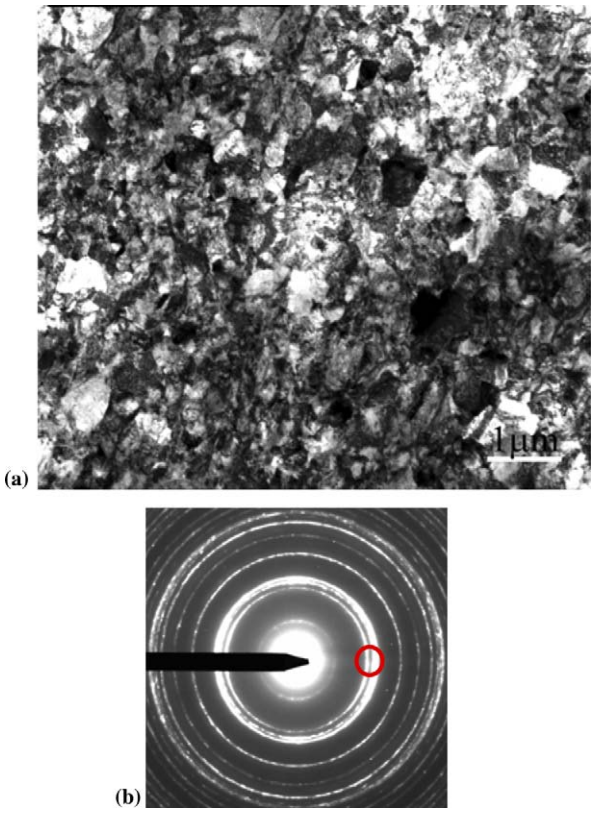

Fig. 17. Deformation shear band grain structure for hat displacement $x = 2$ mm: (a) overall view; (b) diffraction pattern produced by placing the diffraction aperture over most of the shear band width. The microstructure reveals fine grains of ~200 nm similar to that of hat displacement $x = 0.75$ mm. However, diffraction evidence produces a well-developed ring structure indicating fine grain size and randomized texture.

middle region of the shear band with the corresponding diffraction pattern (Fig. 17(b)). Once again a fine-grained microstructure of about ~200 nm is observed. In spite of the larger deformation ($x = 2$ mm) applied here, the grain size within the shear band is approximately the same as that of Fig. 16 (i.e., $x = 0.75$ mm). The diffraction pattern (produced by placing the diffraction aperture over most of the shear band width) corresponding to the ultrafine-grain structure within the band consists of well-defined rings, indicating the presence of small highly misoriented grains. For example, we note the evenly distributed diffracted intensity in the first and the second diffracted rings. A diffraction evidence comparison of Figs. 16(b) and 17(b) suggests the misorientation spectrum appears to increase with increasing deformation of the shear band.

3.3.5. Dark-field imaging of the shear bands

Fig. 18 shows bright- and dark-field images of the shear bands for hat displacement $x = 2.00$ mm. The dark-field image formed using an objective aperture covering a portion of the first and second diffracted ring (see red ring in Fig. 17) reveals grains of the order of 200–250 nm as well as the non-contiguous nature of like-oriented grains. Thus, the structure is considered randomized, and at least a well-dispersed fiber texture is required to account for such diffraction and dark-field observations. Fig. 19 shows similar bright- and dark-field images of the shear bands for hat displacement $x = 0.75$ mm. Dark-field images, formed using the cluster-like diffracted spots (see arrows in Fig. 16), reveal the nearly contiguous nature of like-oriented grains. Thus, the structure while exhibiting a fine grain size of about 200 nm remains strongly textured. Similar observations were also made for ECAP Cu samples [51].

The results described above suggest that the ultrafine-grained microstructure developed during dynamic shear localization resembles that present in materials processed by SPD methods. Indeed, Kim et al. [52] report grain sizes of 200 nm in pure Zr extruded by ECAE. Therefore, it may be speculated that the grain refinement mechanism may be similar, in spite of the fact that the deformation conditions, such as temperature and strain rate, are significantly different for the two processes. For example, the strain rate during ECAP is typically 1 s^{-1}, while it is about 10^4 s^{-1} in the dynamic tests presented in this study. Additionally, the temperature rise during ECAP is less than 100 K, whereas it amounts to about 500–630 K during dynamic tests.

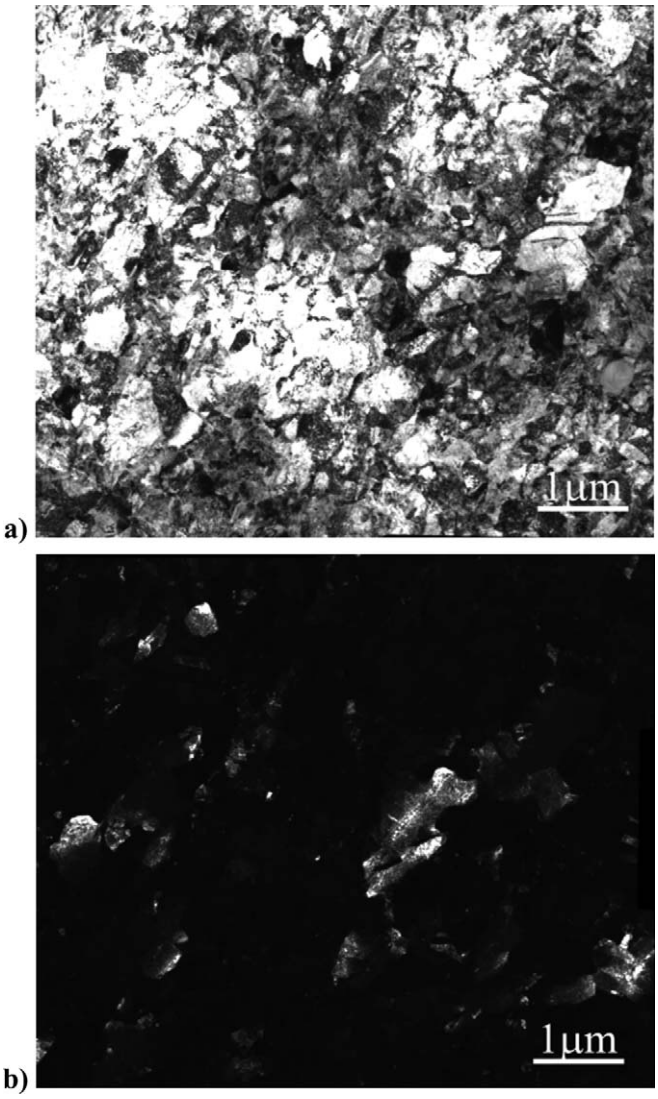

Fig. 18. Bright- and dark-field images of the shear bands for hat displacement $x = 2$ mm. Dark-field image reveals grains even smaller than 200 nm as well as the non-contiguous nature of like-oriented grains. The structure is deemed randomized.

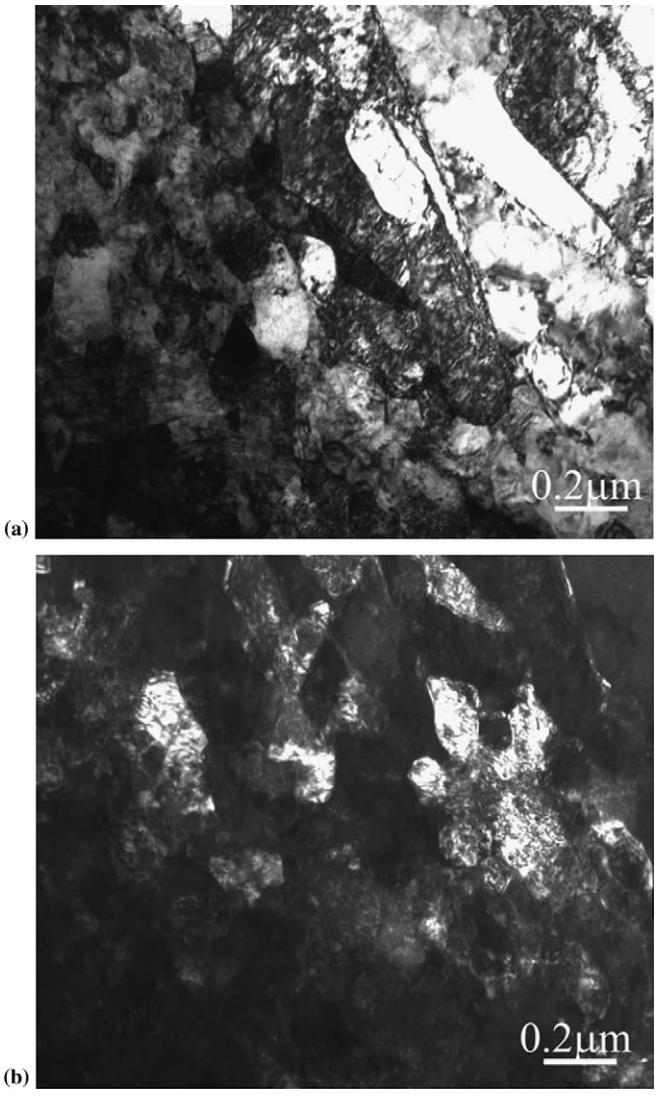

Fig. 19. Bright- and dark-field images of the shear bands for hat displacement $x = 0.75$ mm. Dark-field image reveals the nearly contiguous nature of like-oriented grains. The structure while exhibiting a fine grain size remains strongly textured.

3.4. Constitutive description

Fig. 20(a) shows the stress–strain curves corresponding to the low-strain-rate compression tests performed at room temperature both in the longitudinal and the transverse directions at strain rates of 10^{-3} and $10^{-2}\,s^{-1}$. It can be seen that the strength in the transverse direction is higher than that in the longitudinal direction. As will be described later, this observation may be attributed to a texture effect. The yield stress measured along the longitudinal direction at $10^{-3}\,s^{-1}$, 337 MPa, is consistent with the value given by the manufacturer (352 MPa). Fig. 20(b) shows the dynamic stress–strain curves corresponding also to longitudinal and transverse tests. The yield stress is now approximately 1 GPa. Again, a higher yield stress value is obtained for the transverse direction. The high-strain-rate tests give a lower work hardening due to thermal softening.

Zerilli and Armstrong developed constitutive equations based on microstructural observations for face-centered cubic (fcc), body-centered cubic (bcc), and hcp metals [53–55]. The equations developed show a good match with experimental observations. Eq. (4), which was applied by Meyers et al. to describe the mechanical response of hexagonal materials, relates the yield stress to the strain rate, the plastic strain, temperature, and grain size:

$$\sigma = \sigma_G + C_1\left(\frac{\dot{\varepsilon}_0}{\dot{\varepsilon}}\right)^{-C_3T} + \frac{C_2}{e^{-C_4T}}\varepsilon^n + k_s d^{-\frac{1}{2}} \tag{4}$$

The first term on the right-hand side represents the athermal part of the stress required for plastic deformation. The second and third terms represent the increase of the yield stress related to an increase of strain rate and plastic strain, respectively (athermal part). The last term on the right-hand side represents the Hall–Petch relationship (also

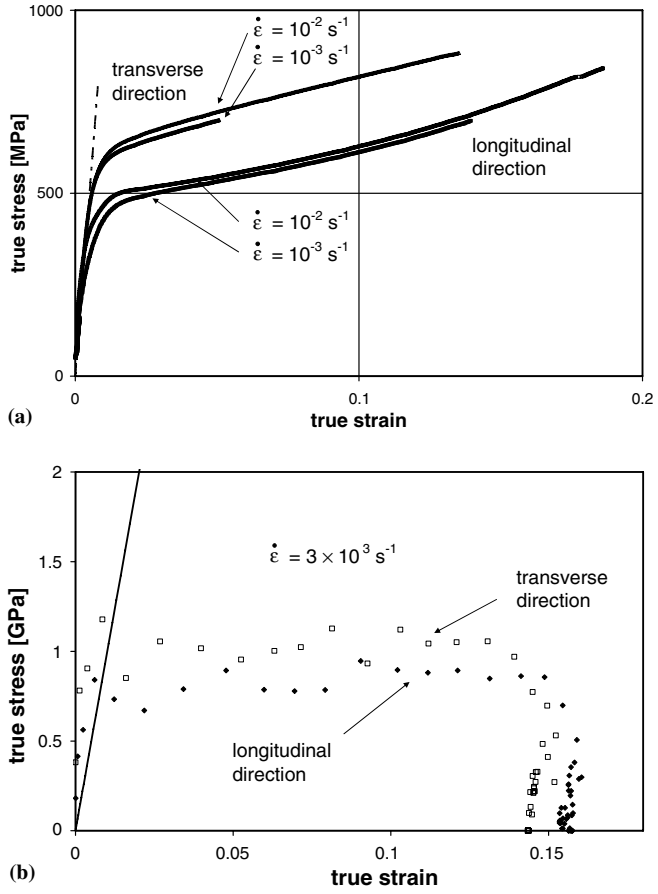

Fig. 20. (a) Quasi-static tensile response in longitudinal and transverse directions and (b) dynamic compressive response in longitudinal and transverse directions.

considered athermal). Both the work hardening and strain rate sensitivity are influenced by the temperature.

Since only room temperature experiments were carried out, the thermal softening was established using results from the literature. For the Hall–Petch parameter, the values estimated by Keeler on tensile tests were used. Fig. 21 illustrates the thermal softening from three different literature sources and the Zerilli–Armstrong fit to the data using the yield stress of the alloy being investigated. The thermal softening parameters used to fit the experimental data were selected to match the results available in the literature. Table 4 provides the fitting parameters for the Zerilli–Armstrong equation.

Table 4
Fitting parameters of the Zerilli–Armstrong equation estimated for zirconium

Fitting parameter	Unit	Estimated value
C_1	MPa	750
C_2	MPa	50
C_3	K^{-1}	0.0002
C_4	K^{-1}	0.0005
$\dot{\varepsilon}_0$	s^{-1}	3500
n	–	0.3
$\sigma_G + \frac{k_s}{\sqrt{d}}$	MPa	50

Assuming adiabatic heating, it is possible to estimate the temperature rise within the shear band using the Zerilli–Armstrong equation. Taking into account that a fraction β of the work done is converted into heat, the following equation for the conservation of energy holds:

$$\rho \cdot c_p \cdot dT = \beta \cdot \sigma \cdot d\varepsilon \tag{5}$$

where ρ is the density of the material, c_p the specific heat capacity, T the temperature, σ the (true) stress, and ε the strain. c_p and σ are both functions of the temperature. σ is additionally a function of strain and temperature. Eq. (5) can be numerically solved by replacing the differential operators by deviations. Using the Zerilli–Armstrong equation, one can obtain the following expression:

$$T = T_i + \frac{\beta}{\rho \cdot c_p} \cdot \int_{T_{ii}}^{T} \left[\sigma_G + C_1 \left(\frac{\dot{\varepsilon}_0}{\dot{\varepsilon}} \right)^{-C_3 T} + \frac{C_2}{e^{-C_4 T}} \varepsilon^n + k_s d^{-1/2} \right] d\varepsilon \tag{6}$$

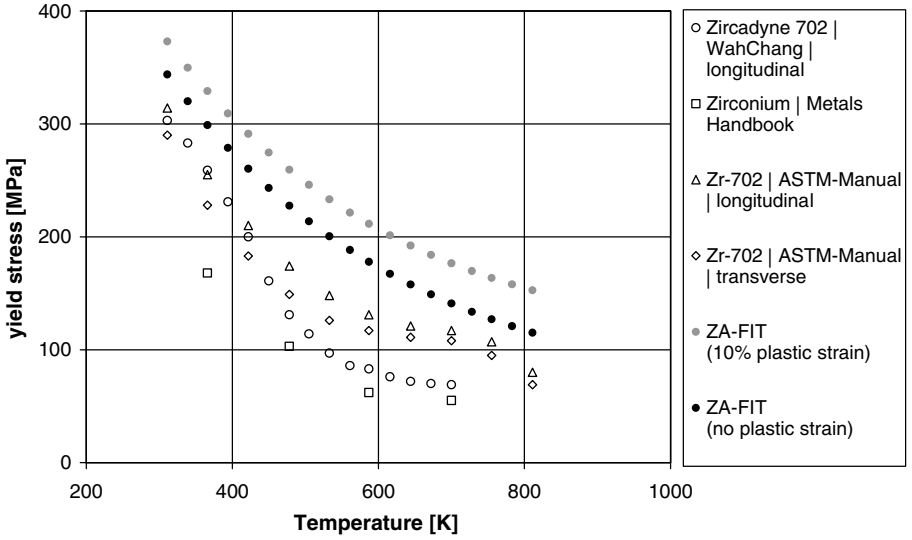

Fig. 21. Effect of temperature on yield and flow stress of zirconium.

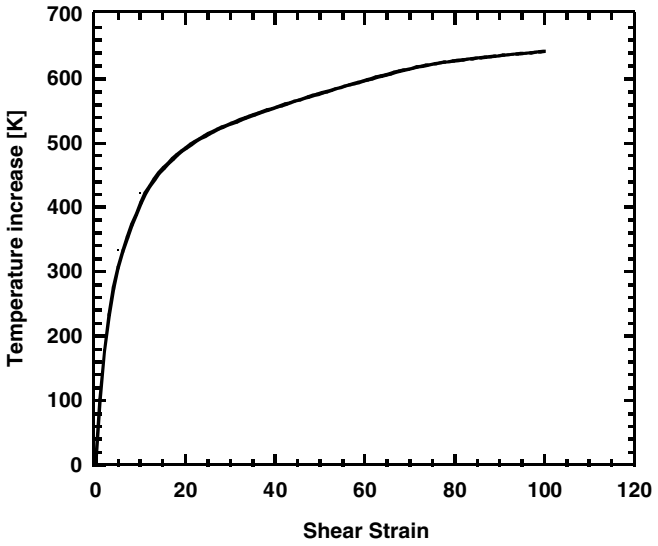

Fig. 22. Calculated temperature rise as a function of shear strain for dynamic deformation (strain rate = 10^4 s^{-1}).

The initial conditions are $\varepsilon_i = 0$, $T_i = 298$ K. Fig. 22 shows the temperature increase caused by plastic deformation at a strain rate of 10^4 s^{-1} and using the constants listed in Table 4. The Taylor factor used was $\beta = 0.9$; it is generally accepted that β varies between 0.85 and 0.95 based on extensive calorimetric measurements (e.g., Ref. [51]). An analysis of Eq. (6) shows that the temperature rise varies with β. Thus, the uncertainty in it is ±5%. A shear strain of $\gamma = 100$ produces a temperature rise $\Delta T = 630$ K and results in a temperature of 930 K. This corresponds to a homologous temperature (T/T_m) of 0.43.

3.5. Modeling of microstructural evolution

The results obtained herein are in full agreement with the early observations by TEM of Grebe et al. [23] for Ti-6Al-4V and Meyers and Pak [25] and Meyers et al. [27] for commercial-purity Ti. Recent results of Chichili et al. [38] also show the formation of an equiaxed ultrafine-grain structure inside the shear band in Ti. Indeed, the response of Zr is very similar to Ti, including the shear band width. The microscopic observations made within areas of intense plastic deformation in other metals (Cu [8,29]; Ta [30–33]; Al alloys [34]) produced by the hat-shaped technique, show the same behavior: the formation of an ultrafine-grain structure. The microstructures for these hcp, fcc, and bcc crystal structures are remarkably similar: approximately equiaxed micrograins with diameters between 0.1 and 0.3 μm.

The sequence of events depicted in Fig. 23 is expected to occur. This sequence was first postulated by Andrade et al. [28] and Meyers et al. [27] and has since then been described in increasing detail. In essence, one starts with a random dislocation distribution (Fig. 23(a)), which is not a low-energy configuration. This random distribution gives way to elongated cells, such as the ones shown in Fig. 17(a). This stage is shown in Fig. 23(b). As the deformation continues and as the misorientation increases, these cells become elongated subgrains (Fig. 23(c)). These elongated structures are seen in many metals subjected to high strains, as reported by Sevillano et al. [7], among others. Hughes and Hansen [49] reported rotations of 30–45° at medium and large strains (cold rolling reductions from 70% to 90%). Hughes et al. [56] made detailed TEM observations of heavily deformed metals and found evolution from configuration b to c in Fig. 23. Similar observations

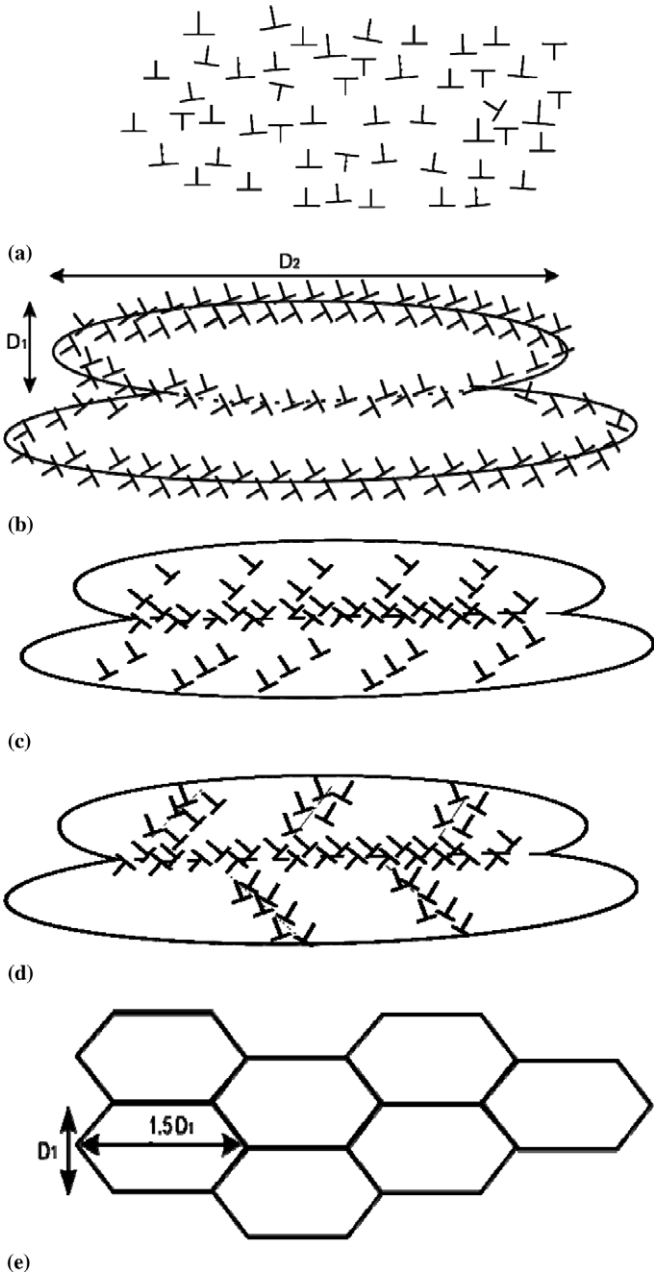

Fig. 23. Schematic of microstructural evolution during severe dynamic plastic deformation. (a) Homogeneous distribution of dislocations; (b) elongated cell formation; (c) dislocation accumulation in subgrain boundaries; (d) breakup of elongated subgrains; and (e) reorientation of subgrain boundaries and formation.

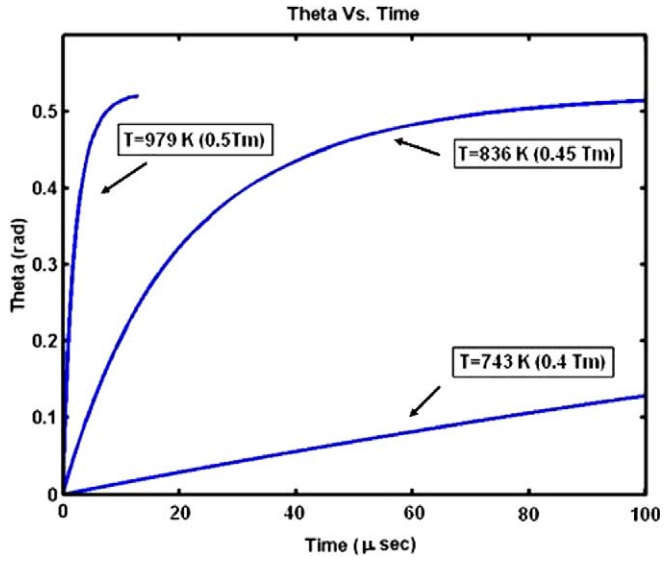

Fig. 24. Rotation of a 200 nm boundary as a function of time for three temperatures.

and analyses were reported by others [56–60]. These elongated subgrains are, in their turn, plastically deformed, leading to further breakup (Fig. 23(d)). Eventually, the elongated subgrains break up into approximately equiaxed micrograins (Fig. 23(e)). This sequence of events, well known for SPD, has received different names: (i) rotational dynamic recrystallization (e.g., Ref. [61]), (ii) formation of geometrically necessary boundaries [56–60], and (iii) continuous recrystallization [62].

Once this equiaxed ultrafine-grain structure is achieved, it has to undergo additional plastic deformation under the imposed conditions. As the grain size is reduced to the 50–200 nm range, the deformation mechanisms operating at conventional grain sizes have to be reexamined. This is an area of much current research, and the concept of grain boundary sources and sinks is gaining importance [63,64]. A step-by-step derivation of grain boundary rotation is provided by Meyers et al. [32], which leads to the following expression:

$$\frac{\tan\theta - \frac{2}{3}\cos\theta}{(1-2\sin\theta)} + \frac{4}{3\sqrt{3}}\ln\frac{\tan\frac{\theta}{2} - 2 - \sqrt{3}}{\tan\frac{\theta}{2} - 2 + \sqrt{3}} + \frac{2}{3} - \frac{4}{3\sqrt{3}}\ln\frac{2+\sqrt{3}}{2-\sqrt{3}} = \frac{4\delta D\gamma}{L_1 kT}t \tag{7}$$

The homologous temperature was made equal to $0.4T_m$, $0.45T_m$, and $0.5T_m$ for a grain side $L_1 = 0.2$ μm. This is a conservative value, since a hexagonal grain with diameter of 0.2 μm would have a side of 0.1 μm. The temperatures are realistic and were obtained from Fig. 22. The most important parameter in Eq. (7) is the grain boundary diffusion coefficient. These values were obtained experimentally by Vieregge and Heriz [65]:

$$\delta D_{GB} = 4.2\times10^{-13}\exp\left[\frac{-167\ \text{kJ mole}^{-1}}{RT}\right](\text{m}^3/\text{s}) \tag{8}$$

The grain boundary width, variously taken as 0.5–1 nm, is not needed, since it is embedded into Eq. (8). The interfacial energy was obtained from Murr [66]. It is taken as 0.725 mJ/m^2. The rate of rotation decreases with increasing θ and asymptotically approaches 30° as $t \to \infty$. The calculation results, shown in Fig. 24, predict significant rotations of the boundary within the deformation time (~50–100 μs) at temperatures between $0.45T_m$ and $0.5T_m$, for micrograin sizes of 0.1–0.3 μm. Thus, the reorientation of grain boundaries can take place during plastic deformation. This does not exclude the possibility of reorientation/accommodation of the grain boundaries during cooling.

4. Conclusions

The purpose of the present work was to investigate the feasibility of developing an ultrafine-grained microstructure in a polycrystalline commercially pure Zr alloy through dynamic shear localization. Dynamic testing was carried out in a split Hopkinson bar at 10^{-4} s^{-1} to shear strains ranging from 30 to 100, and the resulting microstructures were characterized by OM, EBSD, and TEM. The following conclusions may be drawn from this study:

1. Well-defined shear bands were observed in all the specimens tested. The shear band width was found to increase with shear strain, being in the range 9–24 μm. Grains in the vicinity of the shear band undergo moderate distortions and elongate toward the shear direction.
2. The mechanical response was modeled by means of a Zerilli–Armstrong equation for hexagonal materials. This constitutive equation was used to estimate the adiabatic temperature rise inside the shear band as a function of shear strain. It was found that the temperature within the band for the specimens subjected to a shear strain of 100 reaches 930 K. The corresponding homologous temperature is close to 0.43.
3. Grains in the vicinity of the shear band accommodate deformation by undergoing lattice rotations toward a stable orientation under the stress state imposed. Such an orientation was found to be one in which a $\langle 11\bar{2}0\rangle$ direction is aligned with the shear direction and a $(10\bar{1}0)$ plane is parallel to the shear plane. This is consistent with the predominance of prismatic $\{10\bar{1}0\}\langle 11\bar{2}0\rangle$ slip. Additionally, the need for adjacent grains to achieve compatible deformation leads to the formation of a weak $\langle 11\bar{2}0\rangle$ fiber texture.
4. An ultrafine-grained microstructure, with highly misoriented grains of an average diameter of 200 nm, develops within the shear band. This microstructure resembles that characteristic of materials processed by SPD methods such as ECAE.
5. A mechanism for the formation of the ultrafine grain size proposed earlier is applied to zirconium, and it is demonstrated that the rotation of grain boundaries with sizes of 0.1–0.2 μm can be accomplished in times

consistent with the deformation times inside the shear band. It is proposed that the mechanism of grain refinement in adiabatic shear localization is similar to that taking place in SPD. This reinforces the earlier proposal [35] based on observations and analysis carried out for stainless steel.

Acknowledgements

J.M.G. is grateful to Profs. D. Löhe and O. Vöhringer for giving him the opportunity to carry out his Diplomarbeit at UCSD. Mr. Franck Grignon and Dr. Matthew Schneider are acknowledged for fruitful discussions and for helping out with dynamic testing. Valuable help from S. Barrabes in polishing zirconium is gratefully acknowledged. The authors are grateful to the Servicio de Microscopía of the Universidad Politécnica of Valencia, Spain, for kindly allowing M.T.P. use the EBSD facilities. Support by the National Science Foundation under Grants DMR 0419222 and CMS-0210173 (NIRT) is acknowledged.

References

[1] Gleiter H. Prog Mater Sci 1989;33:223.
[2] Birringer R. Mater Sci Eng 1989;A117:33.
[3] Gleiter H. Nanostruct Mater 1992;1:1.
[4] Suryanarayana C. Int Mater Res 1995;40:41.
[5] Suryanarayana C, Koch CC. Hyperfine Interact 2000;130:5.
[6] Valiev RZ, Islamgaliev RK, Alexandrov IV. Prog Mater Sci 2000;45:103.
[7] Sevillano JG, van Houtte P, Aernoudt E. Prog Mater Sci 1981;25:69.
[8] Smirnova NA, Levit VI, Pilyugin VI, Kuznetsov RI, Davydova LS, Sazonova VA. Fiz Metal Metalloved 1986;61:1170.
[9] Horita Z, Smith DJ, Furukawa M, Nemoto M, Valiev RZ, Langdon TG. J Mater Res 1996;11:1880.
[10] Alexandrov IV, Zhu YT, Lowe TR, Islamgaliev RK, Valiev RZ. Nanostruct Mater 1998;10:45.
[11] Alexandrov IV, Zhu YT, Lowe TR, Islamgaliev RK, Valiev RZ. Metall Mater Trans 1998;29A:2253.
[12] Alexandrov IV, Zhu YT, Lowe TC, Islamgaliev RK, Valiev RZ. Powder Metall 1998;11:41.
[13] Stolyarov VV, Zhu YT, Lowe TC, Islamgaliev RK, Valiev RZ. Mater Sci Eng 2000;A282:78.
[14] Zhilyaev AP, Lee S, Nurislamova GV, Valiev RZ, Langdon TG. Scripta Mater 2001;44:2758.
[15] Zhilyaev AP, Nurislamova GV, Kim BK, Baró MD, Szpunar JA, Langdon TG. Acta Mater 2003;51:753.
[16] Iwahashi Y, Horita Z, Nemoto M, Langdon TG. Acta Mater 1998;46:3317.
[17] Nemoto M, Horita Z, Furukawa M, Langdon TG. Metall Mater Int 1998;4:1181.
[18] Langdon TG, Furukawa M, Nemoto M, Horita Z. J Miner Metal Mater Soc 2000;52:30.
[19] Furukawa M, Horita Z, Nemoto M, Langdon TG. J Mater Sci 2001;36:2835.
[20] Horita Z, Fujinami T, Langdon TG. Mater Sci Eng 2001;A318:34.
[21] Horita Z, Lee S, Ota S, Neishi K, Langdon TG. Superplast Adv Mater Icsam-2000 2001;357:471.
[22] Furukawa M, Horita Z, Nemoto M, Valiev RZ, Langdon TG. Mater Charact 1996;37:277.
[23] Grebe A, Pak H-R, Meyers MA. Metall Trans A 1985;16A:761.
[24] Pak H-R, Wittman CL, Meyers MA. In: Murr LE, Staudhammer KP, Meyers MA, editors. Metallurgical applications of shock-wave and high-strain-rate phenomena. New York: Marcel Dekker; 1986. p. 60.
[25] Meyers MA, Pak H-R. Acta Metall 1986;34:2493.
[26] Beatty JH, Meyer LW, Meyers MA, Nemat-Nasser S. Shock-wave and high-strain rate phenomena in materials. New York: Marcel Dekker; 1992.
[27] Meyers MA, Subhash G, Kad BK, Prasad L. Mech Mater 1994;17:175.
[28] Andrade UR, Meyers MA, Vecchio KS, Chokshi AH. Acta Metall Mater 1994;42:3183.
[29] Meyers MA, Andrade U, Chokshi AH. Metall Mater Trans A 1995;26A:2881.
[30] Nesterenko VF, Meyers MA, LaSalvia JC, Bondar MP, Chen Y-J, Lukyanov YL. Mater Sci Eng 1997;A229:23.
[31] Chen Y-J, Meyers MA, Nesterenko VF. Mater Sci Eng 1999;A268:70.
[32] Meyers MA, LaSalvia JC, Nesterenko VF, Chen YJ, Kad BK. In: McNelley TR, editor. Rex '96, Monterey; 1997. p. 27.
[33] Meyers MA, Nesterenko VF, LaSalvia JC, Xue Q. Mater Sci Eng 2001;A317:204.
[34] Xu YB, Zhong WL, Chen YJ, Shen LT, Liu Q, Bai YL, Meyers MA. Mater Sci Eng 2001;A299:287.
[35] Meyers MA, Perez-Prado MT, Xue Q, Xu Y, McNelley TR. Acta Mater 2003;51:1307.
[36] Meunier Y, Roux R, Moureaud J. In: Shock-wave and high-strain rate phenomena in materials. New York: Marcel Dekker; 1992. p. 637.
[37] Li Q, Xu YB, Lai ZH, Shen LT, Bai YL. Mater Sci Eng 2000;A276:127.
[38] Chichili DR, Ramesh KT, Hemker KJ. JMPS 2004;52:1889.
[39] Xue Q, Liao XZ, Zhu YT, Gray III GT. Mater Sci Eng A 2005;410:252–6.
[40] Meyer LW, Manwaring S. In: Metallurgical applications of shock-wave and high-strain-rate phenomena. New York: Marcel Dekker; 1986. p. 657.
[41] Gebert G-M. Diplomarbeit, U Karlsruhe (TH), 2004.
[42] Meyers MA. Dynamic behavior of materials. Wiley; 1994.
[43] Adams BL, Wright SI, Kunze K. Metall Trans A 1993;24A:819.
[44] Schwarz AJ, Kumar M, Adams BL, editors. Electron backscatter diffraction in materials science. New York: Kluwer/Plenum; 2000.
[45] Randle V. Microtexture determination and its applications. London: Institute of Metals; 1992.
[46] Ashby MF, Jones DRH. Engineering materials. Butterworth-Heinemann; 1996. p. 87.
[47] Armstrong RW. In: Bunshah RF, editor. Advances in materials research, vol. 5. New York: Wiley; 1971. p. 101.
[48] Tenckhoff E. Deformation mechanisms, texture, and anisotropy in zirconium and zircaloy. ASTM Special Publication 966; 1988.
[49] Hughes DA, Hansen N. Acta Mater 1997;45:3871.
[50] Pe'rez-Prado MT, Hines JA, Vecchio KS. Acta Mater 2001;49:2905.
[51] Clareborough LM, Hargreaves ME. Prog Metal Phys 1959;8:1.
[52] Kim HS, Joo D-H, Kim M-H, Hwang S-K, Kwun S-I, Chae S-W. Mater Sci Technol 2003;19:403.
[53] Zerilli FJ, Armstrong RW. J Appl Phys 1987;61:1816.
[54] Zerilli FJ, Armstrong RW. J Appl Phys 1990;68:1580.
[55] Zerilli FJ, Armstrong RW. In: AIP conference proceedings (no. 370), Seattle (WA), 1995. AIP; 1996. p. 315.
[56] Hughes DA, Lebensohn RA, Wenk HR, Kumar A. Proc R Soc Lond A 2000;456:921.
[57] Kuhlmann-Wilsdorf D, Hansen N. Scripta Metall Mater 1991;25:1557.
[58] Bay B, Hansen N, Hughes DA, Kuhlmann-Wilsdorf D. Acta Metall Mater 1992;40:205.
[59] Liu Q, Hansen N. Scripta Metall Mater 1995;32:1289.
[60] Hughes DA, Chrzan DC, Liu Q, Hansen N. Phys Rev Lett 1998;81:4664.

[61] Derby B. Acta Metall 1991;39:955.
[62] Humphreys FJ, Hatherly M. Recrystallization and related annealing phenomena. Oxford: Pergamon; 1995.
[63] Yamakov D, Wolf D, Phillpot SR, Mukherjee AK, Gleiter H. Nature Mater 2002;1:1.
[64] Froseth AG, Derlet H, Van Swygenhoven H. Acta Mater 2004;52: 4025.
[65] Vieregge K, Heriz C. J Nucl Mater 1990;173:118.
[66] Murr LE. Interfacial phenomena in metals and alloys. Addison-Wesley; 1975.